

Custom-Designed III-V Semiconductor Microstructures Scaled to the Ultimate Physical Limit: Ultrathin-Layer $GaAs/AlAs$ Superlattices and Delta- (Monolayer) Doping in $GaAs/Al_xGa_{1-x}As$ Structures

K. Ploog and R. Muralidharan*

Max-Planck Institut für Festkörperforschung, D-7000 Stuttgart 80, FRG

ABSTRACT

Two prototype artificially-layered semiconductor structures are presented in which the concept of microscopical structuring of solids is scaled to its ultimate physical limit normal to the crystal surface. In both the $(GaAs)_1/(AlAs)_1$ monolayer superlattice and in the delta- (or monolayer) doped $GaAs/Al_xGa_{1-x}As$ structures, which have been grown by molecular beam epitaxy, the characteristic material lengths have reached a spatial extent normal to the surface of less than the lattice constant. The $(GaAs)_m/(AlAs)_n$ ultrathin-layer superlattices exhibit novel optical properties due to the indirect-gap nature of the constituent $AlAs$ layers. The minority-carrier lifetimes can be tailored over four orders of magnitude by appropriately designing the superlattice configuration. This feature opens up new fields of application in lasers and in nonlinear photonic and optoelectronic devices. The narrow buried doping channel in delta-doped $GaAs$ layers and in $GaAs/Al_xGa_{1-x}As$ structures leads to a significant improvement of the electrical properties. Based on this concept, nonalloyed ohmic contacts, field-effect transistors with very high transconductance, unpinned $GaAs$ surfaces for MOS devices, and electron mobilities as high as $10^7 \text{ cm}^2\text{V}^{-1}\text{s}^{-1}$ have been fabricated.

1. INTRODUCTION

Molecular beam epitaxy (MBE) of custom-designed microstructures has reached a status where monolayer dimensions in artificially-layered semiconductors are being routinely controlled to form a new class of materials with accurately tailored electrical and

Received 21 July 1989

*On leave from Solid State Physics Laboratory, Delhi-110 007, India

optical properties^{1,2}. The unique capabilities of MBE in terms of spatially resolved materials synthesis has stimulated the inspiration of device engineers to design a whole new generation of electronic and photonic devices based on the concept of band gap engineering^{3,4}. This concept, also called wavefunction or density-of-states engineering^{5,6}, respectively, relies on the arbitrary modulation of band-edge potentials in semiconductors through the abrupt change of composition (for example, *GaAs/AlAs*, *GaSb/InAs*, *Si/Ge*, etc.) or of dopant concentration. The microscopic structuring or engineering of semiconducting solids to within atomic dimensions is thus achieved by the incorporation of interfaces (consisting of abrupt homo or heterojunctions) into a crystal in well-defined geometrical and spatial arrangements. The electrical and optical properties are then defined locally, and the phenomena related to extremely small dimensions (quantum size effects) become more important than the actual chemical properties of the materials involved.

In this article we present two prototype artificially-layered semiconductor structures where the concept of microscopical structuring of solids is scaled to its ultimate physical limit normal to the crystal surface, i.e., *GaAs/AlAs* ultrathin-layer superlattices and delta-doping (or monolayer doping) in *GaAs* and *Al_xGa_{1-x}As*. Each constituent layer in the (*GaAs*)₁/*(AlAs)*₁ monolayer superlattice and also the narrow buried delta-doping channel, for example, in *GaAs*, have a spatial extent normal to the surface of less than the lattice constant of the respective bulk material. Both the *GaAs/AlAs* ultrathin-layer superlattice as well as the delta-doped *GaAs/Al_xGa_{1-x}As* structures have recently become very important for fundamental studies and for application in advanced semiconductor device concepts.

2. FUNDAMENTALS OF MBE

The fabrication of custom-designed microstructures, where the desired potential differences are defined locally by the accurate positioning of heterojunctions, requires advanced epitaxial crystal growth techniques, such as MBE. The particular merits of MBE are that ultrathin films can be grown with precise control over thickness, composition, and doping level⁵⁻⁸. The technique allows atomic layer-by-layer deposition in a 2-D growth process, and crystalline materials in alternating layers of arbitrary composition and only a few atomic layers thick can be formed. Figure 1(a) shows schematically the fundamentals for MBE growth of III-V semiconductors. The MBE process consists of a co-evaporation of the constituent elements (*Al*, *Ga*, *In*, *P*, *As*, *Sb*) of the epitaxial layer and dopants (mainly *Si* for *n*-type and *Be* for *p*-type doping) onto a heated crystalline substrate where they react chemically under ultrahigh-vacuum (UHV) conditions (Fig. 1(b)). The composition of the layer and its doping level depend on the relative arrival rate of the constituent elements which in turn depends on the evaporation rate of the appropriate sources. Accurately controlled temperatures (to within $\pm 0.1^\circ$ at 1000°C) thus have a direct controllable effect upon the growth process.

The group III elements are always supplied as monomers by evaporation from the respective liquid element and have a unity sticking coefficient over most of the substrate temperature range used for film growth (for example, 500 to 650°C for *GaAs*). The group V elements, on the other hand, can be supplied as tetramers (*P₄*, *As₄*, *Sb₄*) by sublimation from the respective solid element or as dimers (*P₂*, *As₂*, *Sb₂*) by dissociating the tetrameric molecules in a two-zone furnace. The growth rate (typically 0.5 to 1.5 $\mu\text{m/hr}$) is chosen, low enough that migration of the impinging species on the growing surface to the appropriate lattice sites is ensured without incorporating crystalline defects. Simple mechanical

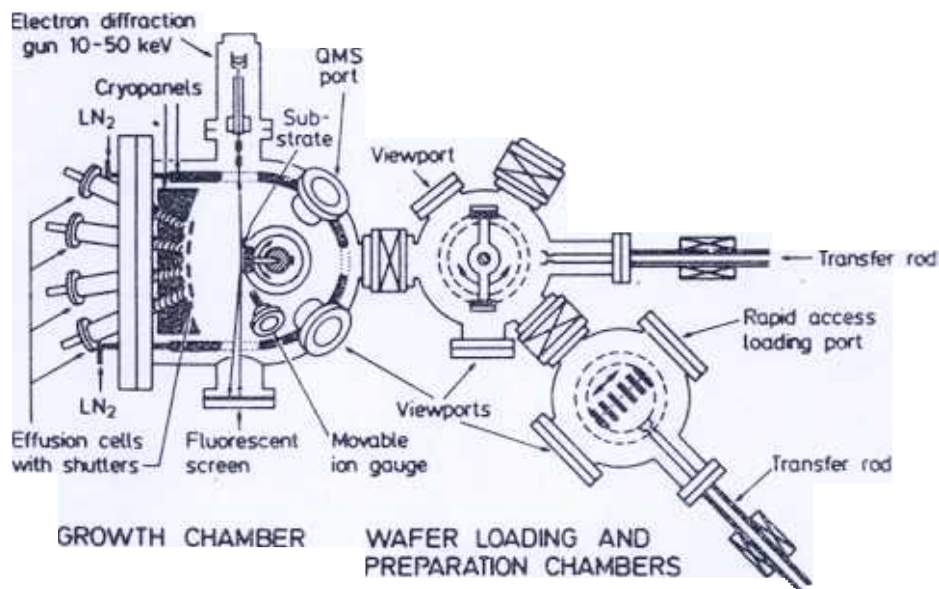
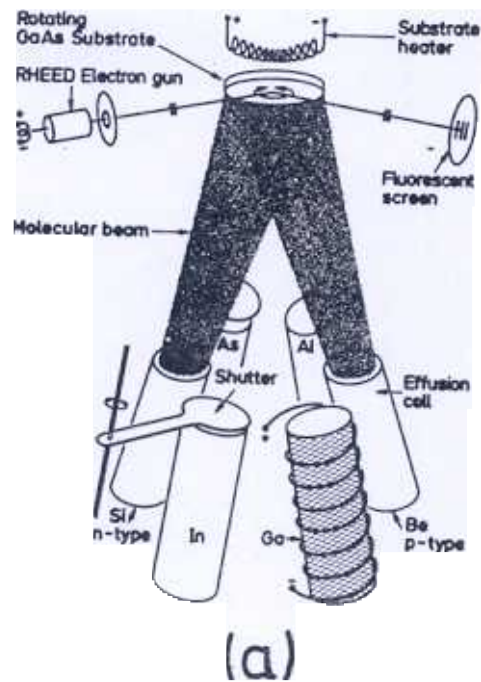


Figure 1. (a) Schematic illustration of evaporation and deposition process during MBE of III-V compounds and (b) schematic cross-section of UHV system designed for MBE comprising reaction chamber, preparation chamber and load-lock chamber.

shutters in front of the evaporation sources are used to interrupt the beam fluxes to start and stop deposition and doping. Due to the slow growth rate, i.e., one monolayer/s, changes in composition and doping can thus be abrupt on an atomic scale. The transmission electron micrograph (TEM) of a GaAs superlattice displayed in Fig. 2 demonstrates that this independent and accurate control of the individual beam sources allows the precise fabrication of artificially-layered semiconductor structures on an atomic scale.

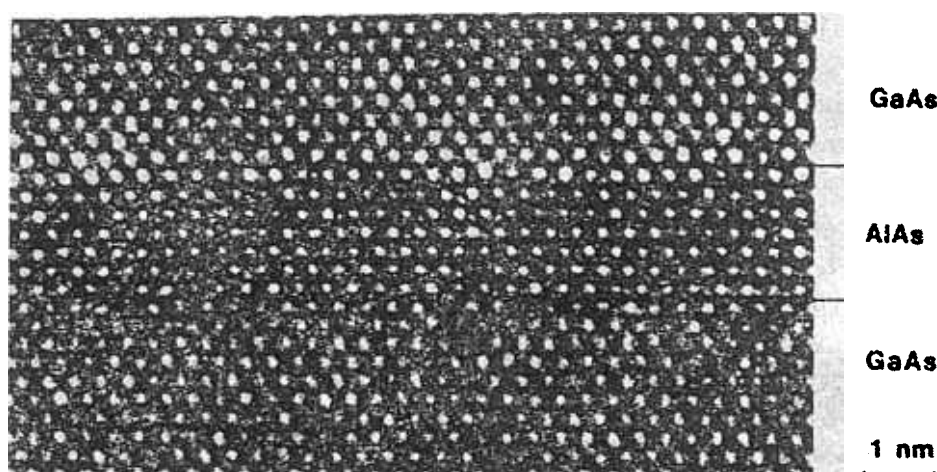


Figure 2. High-resolution lattice image of *GaAs/AlAs* superlattice obtained by TEM.

The stoichiometry of most III-V semiconductors during MBE growth is self-regulating as long as excess group V element molecules are impinging on the growing surface. The excess group V species do not stick on the heated substrate surface, and the growth rate is essentially determined by the arrival rates of group III elements. The simplicity of the MBE process allows composition control from $x = 0$ to $x = 1$ in $Al_xGa_{1-x}As$, $Ga_xIn_{1-x}As$, etc., with a precision of ± 0.001 and both *n*- and *p*-type doping control from the 10^{14} cm^{-3} to the 10^{19} cm^{-3} range with a precision of a few per cent. The accuracy is largely determined by the care with which the growth rate and doping level were precisely calibrated in test layers.

Most of the advanced MBE systems consist of three basic UHV building blocks (the growth chamber, the sample preparation chamber, and the load-lock chamber) which are separately pumped and interconnected via large diameter channels and isolation valves (Fig. 1(b)). High-quality layered semiconductor structures require background vacuum in the low 10^{-11} torr range to avoid incorporation of impurities into the growing layers. Therefore, extensive liquid nitrogen cryoshrouds are used around the substrate to achieve locally much lower background pressures of condensable species. The starting materials for the growth of III-V semiconductors are evaporated in resistively heated effusion cells made of pyrolytic boron nitride (PBN) which operate at temperatures up to 1400°C .

In general MBE growth of III-V semiconductors is performed on (001) oriented substrate slices about 300 to 500 μm thick. The preparation of the growth face of the substrate from the polishing stage to the *in situ* cleaning stage in the MBE system is of crucial importance for epitaxial growth of ultrathin layers and heterostructures with high purity and crystal perfection and with accurately controlled interfaces on an atomic scale. The substrate surface should be free of crystallographic defects and clean on an atomic scale with less than 0.01 monolayer of impurities. Various cleaning methods have been described for *GaAs* and *InP* which are the most important substrate materials for deposition of III-V semiconductors. The first step always involves chemical etching, which leaves the surface covered with some kind of a protective oxide. After insertion in the MBE system this oxide is removed by heating carried out in a beam of the group V element.

The most important method to monitor *in situ* surface crystallography and kinetics during MBE growth is reflection high energy electron diffraction (RHEED) operated at 10 to 50 keV in the small glancing angle reflection mode (Fig. 3). The diffraction pattern on the fluorescent screen contains information from the topmost nanometer of the deposited

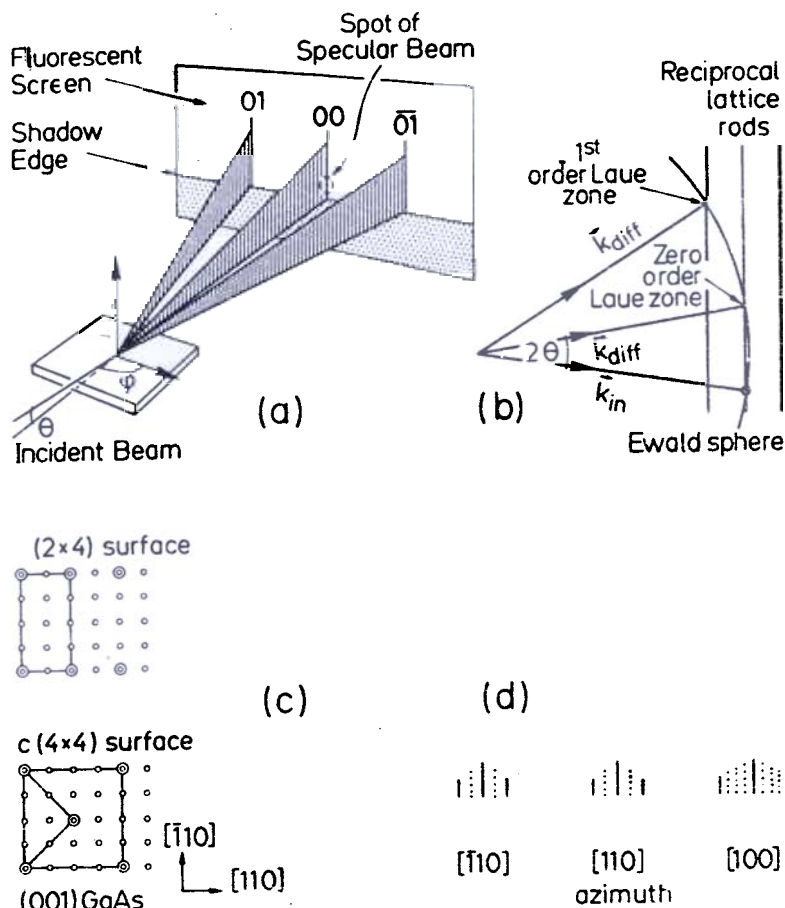


Figure 3. Schematic illustration of (a) electron diffraction with grazing-angle incidence (RHEED) during MBE, (b) Ewald construction to interpret the diffraction conditions, (c) surface unit cell, and (d) diffraction patterns of reconstructed (2×4) surface.

material that can be related to the topography and structure of the growing surface. The specific surface reconstruction can be identified and correlated to the surface stoichiometry which is an important growth parameter. In addition, the temporal intensity oscillations observed in the features of the RHEED pattern are used to study MBE growth dynamics and the formation of hetero-interfaces in multilayered structures^{9,10}. The periodic intensity oscillations in the specularly reflected beam of the RHEED pattern shown in Fig. 4

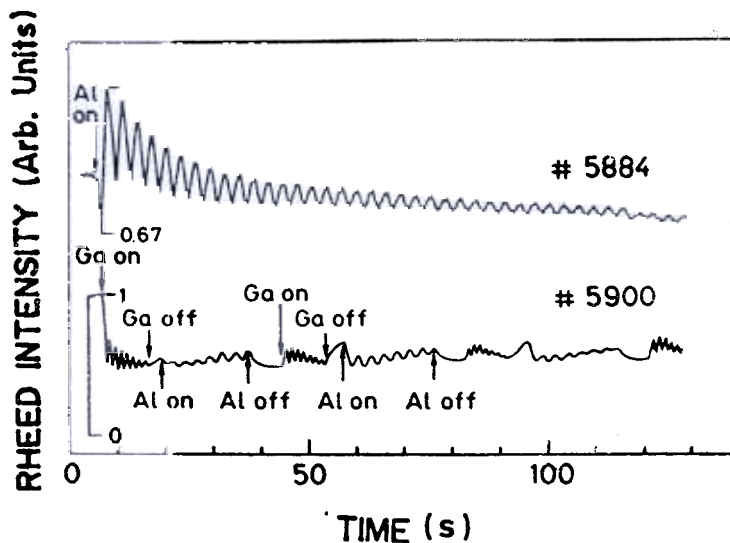


Figure 4. Periodic intensity oscillations of the specularly reflected electron beam in the RHEED pattern as a function of time during growth of GaAs/AlAs multilayers.

provides direct evidence that MBE growth occurs predominantly in a 2-D layer-by-layer growth mode. The period of the intensity oscillations corresponds exactly to the time required to grow a monolayer of *GaAs* (i.e., a complete layer of *Ga* plus a complete layer of *As*), *AlAs*, or $Al_xGa_{1-x}As$. To a first approximation we can assume that the oscillation amplitude reaches its maximum when the monolayer is completed (maximum reflection). The method is now widely used to monitor and to calibrate absolute growth rates in real-time with monolayer resolution.

3. *GaAs/AlAs* SHORT-PERIOD AND ULTRATHIN-LAYER SUPERLATTICES

The research activities on *GaAs/AlAs* short-period superlattices (SPS) were initiated by some detrimental structural, electrical, and optical properties of the ternary alloy $Al_xGa_{1-x}As$. First, the interface roughness for growth of binary *GaAs* or *AlAs* on the ternary alloy¹⁰⁻¹⁵ yields inferior excitonic and transport properties. Second, the electrical properties of *n*-type $Al_xGa_{1-x}As$ for $0.2 < x < 0.43$ are controlled by a deep donor ('DX centre') in addition to the hydrogen-like shallow donor due to the peculiar band structure of the alloy¹⁶⁻¹⁸. Third, the *X*-minimum of the conduction band becomes the lowest¹⁹ one when $x > 0.43$ (at 4 K), and thus an indirect bandgap of the alloy results. The investigations of ultrathin-layer $(GaAs)_m/(AlAs)_n$ superlattices (UTLS) with (m, n) from 10 down to 1 were motivated by the possibilities to shift the confined particle states of the Γ , *L* and *X* valleys of the conduction band (and also of Γ of the valence band) to high enough energy to create radiative size-determined 'direct-indirect' transitions exceeding in energy the bulk direct-indirect transitions²⁰ of the ternary alloy $Al_xGa_{1-x}As$ at $x \approx 0.43$. The all-binary *GaAs/AlAs* SPS and UTLS are thus considered as possible substitutes for the random ternary alloy in advanced device structures. In addition, the electronic properties of these superlattices, which are in the transition regime between the extremes of quantum well behaviour for period length > 8 nm (i.e., $m, n > 15$) and of a possible alloy-like behaviour of monolayer superlattices, are not completely understood.

Confinement layers composed of SPS A_mB_n with $5 \leq (m, n) \leq 10$ play an important role for highly improved optical properties of *GaAs*, *GaSb*, and $Ga_{0.47}In_{0.53}As$ quantum wells²¹⁻²³. Figure 5(a) shows schematically the real-space energy band diagram of a quantum well confined by SPS barriers. Also indicated in this figure is the process of carrier injection and vertical transport in the SPS towards the quantum well and the process of radiative electron-hole recombination²⁴. The SPS barriers consist of all-binary *GaAs/AlAs* for *GaAs* quantum wells, of all-binary *GaSb/AlSb* for *GaSb* quantum wells, and of all-ternary $Ga_{0.47}In_{0.53}As/Al_{0.48}In_{0.52}As$ for $Ga_{0.47}In_{0.53}As$ quantum wells lattice matched to *InP*. The effective barrier height for carrier confinement in the quantum wells is adjusted by the appropriate choice of the layer thickness of the lower-gap material in the SPS. The observed improvement of the optical properties of SPS-confined quantum wells is due to (a) the removal of substrate defects by the SPS layer, (b) the amelioration of the interface between quantum well and barrier, and (c) the modification of the dynamics of photoexcited carriers in the SPS barrier. In particular for *GaSb* and for $Ga_{0.47}In_{0.53}As$ quantum wells we have provided the first direct evidence for intrinsic exciton recombination by application of SPS barriers^{22,23}. Detailed studies of the dynamics of photoexcited carriers sinking into SPS-confined enlarged *GaAs* quantum well have clearly demonstrated an efficient vertical transport of electrons and holes through the thin *AlAs* barriers of the SPS²⁴⁻²⁶. In addition, the recombination lifetime of photoexcited carriers in *GaAs* quantum wells is significantly improved by the application of SPS barriers²⁷.

heterostructure is reduced to less than 15 min. An additional 15 min for wafer exchange and heat and cool time makes a total of 30 min throughput time per 2-in high-quality heterostructure wafer grown by MBE.

The improved dynamics of injected carriers and their efficient trapping by the enlarged well make the SPS-confined quantum wells very attractive for application in newly designed heterostructure lasers with separate superlattice waveguide and superlattice barriers. Figure 5(b) shows schematically how a grading of the effective band gap can be achieved by gradually changing the width of the *GaAs* wells in the SPS³⁰. Recently, graded-index waveguide-separate confinement heterostructure (GRIN-SCH) laser diodes with a very low threshold current density have been fabricated³¹, where the graded-index waveguide was constructed by all-binary *GaAs/AlAs* SPS with gradually changed *GaAs* layer thicknesses (from 1.8 to 3.3 nm at eight intervals of six periods with a constant *AlAs* barrier width of 1.9 nm). Figure 6 shows schematically the energy band diagram of this

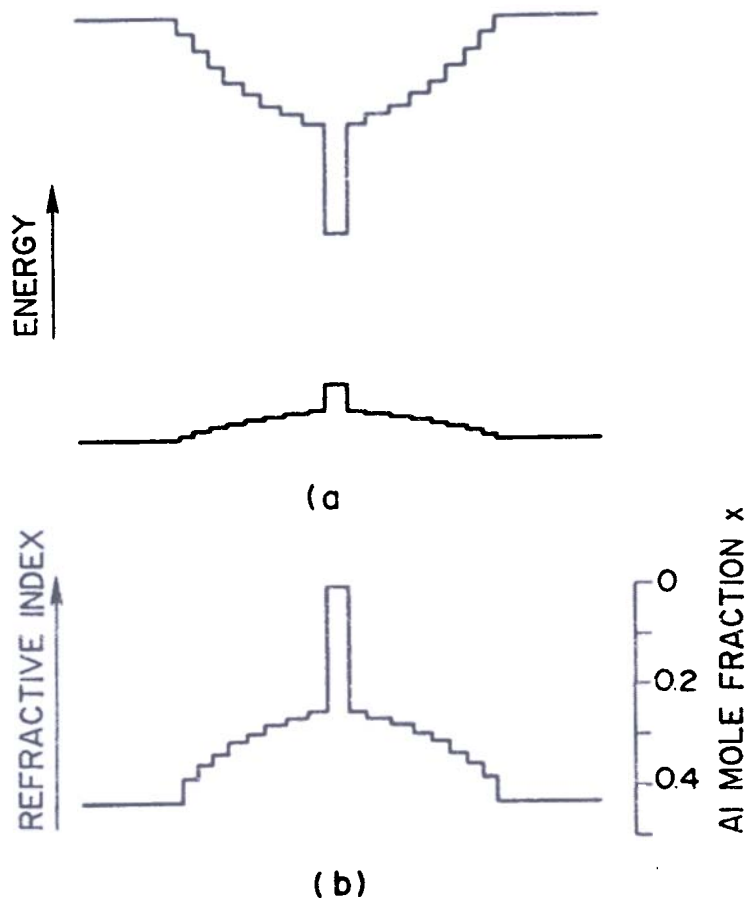


Figure 6. Schematic diagrams of (a) real-space energy bands, and (b) refractive index profile of a GRIN-SCH laser structure with graded-layer thickness SPS waveguide³¹.

GRIN-SCH laser structure having an $Al_{0.43}Ga_{0.57}As$ cladding layer and the corresponding refractive index profile. When *n*- or *p*-doped SPS confinement layers are required, this can be achieved by selectively doping the *GaAs* regions of the SPS³².

Other configurations of heterostructure laser diodes using all-binary *GaAs/AlAs* SPS and UTLS for the cladding, waveguide and barrier regions are schematically depicted in Fig. 7 by means of their conduction band edges³³. Note that in the separate confinement heterostructure (SCH) of configuration (Fig. 7(c)) even the active region of the laser consists of a *GaAs/AlAs* SPS³⁴ yielding an average *Al* mole fraction of $\bar{x} = 0.17$ and thus an

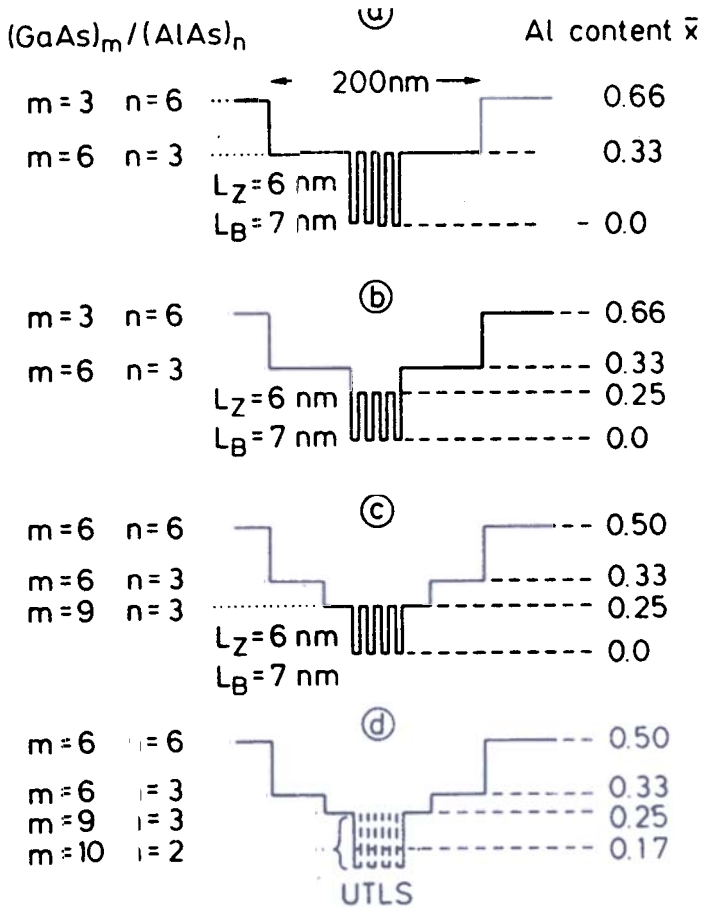


Figure 7. Different configurations of heterostructure lasers using all-binary GaAs/AlAs SPS and UTLS for the cladding, waveguide and barrier region illustrated by means of the real-space conduction band edges.

emission wavelength below 790 nm. The performance of all these laser structures with respect to threshold current and temperature dependence is comparable or even superior to the best conventional QW laser structures. However, the simple description of GaAs/AlAs SPS and UTLS in terms of the average effective alloy composition is not adequate for a detailed understanding of the device physics. This aspect will be discussed in the following paragraphs.

The recent progress in the control of interface quality using RHEED intensity oscillation and growth interruption has led^{35,36} to the successful growth of ultrathin-layer $(GaAs)_m/(AlAs)_n$ superlattices with $1 < (m, n) < 10$. Growth of these superlattices was achieved by monitoring each deposited GaAs and AlAs monolayer from the RHEED oscillation period, interrupting the group III element flux at $(m, n) = 1, 2, 3, \dots$ and allowing the RHEED intensity to recover almost to its initial value, and then depositing the next layer. The well-ordered periodic layer-by-layer arrangement of Ga and Al atoms on the appropriate lattice sites in [001] direction manifests itself in the appearance of distinct satellite peaks around the (002) and (004) reflections of the x-ray diffraction patterns³⁷.

The $(GaAs)_m/(AlAs)_n$ UTLS with low (m, n) values are expected to exhibit not the well-described confined particle states associated with quantum wells but minibands parallel to the layer sequence within which carriers propagate normal to the quantum well plane^{38,39}. Due to the indirect-gap nature of the AlAs barriers, however, the gradual transition of $(GaAs)_m/(AlAs)_n$ superlattices from the well-understood quantum well behaviour for $(m, n) > 15$ to the $(GaAs)_1/(AlAs)_1$ monolayer superlattice can produce either type I

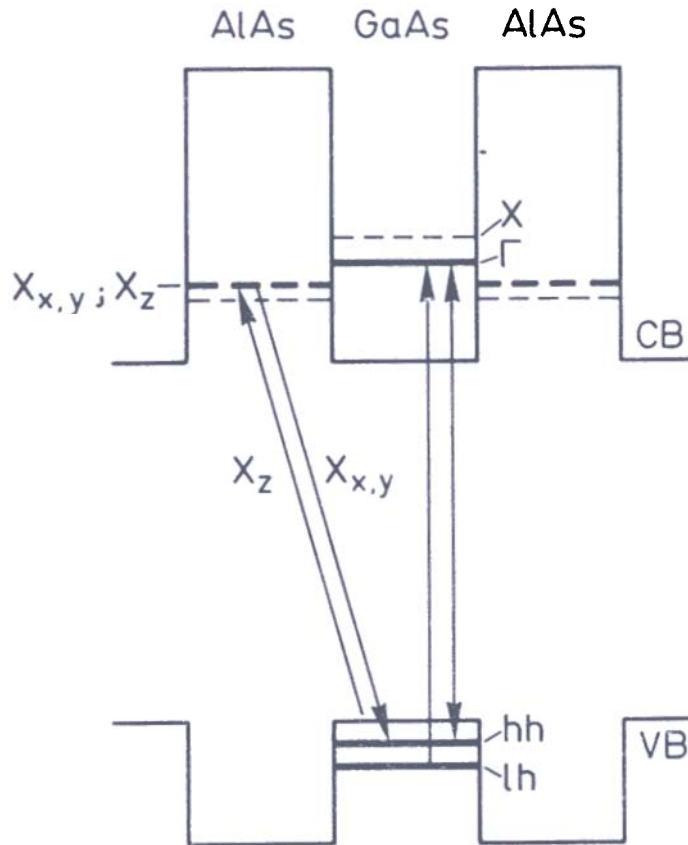


Figure 8. Schematic real-space energy band diagram of *GaAs/AlAs* superlattice to illustrate the type I or type II behavior of the optical properties, depending on the relative position of the Γ - and X -point conduction band minima.

superlattices, where the electrons and holes are confined in the same (*GaAs*) layer, or type II superlattices, characterised by the spatial separation of electrons and holes with electrons confined in the *AlAs* 'barrier' region and holes in the *GaAs* well (Fig. 8)³⁷. The type II behaviour was first observed in *GaSb/InAs* quantum wells where it originates from the peculiar arrangement of the conduction and valence band discontinuities³⁹. In the *GaAs/AlAs* system the essential conditions are that the *AlAs* barrier material is indirect and that the X -point conduction band minima in the barriers lie at lower energy than the Γ minima in the wells, which can be achieved by increasing the Γ confinement energy in very narrow wells³⁹. Note, however, that the simultaneous reduction of the barrier width also leads to an increase of the confinement of the X states of *AlAs* and thus pushes them up in energy. For $m = n$ the transition from type I to type II behaviour in $(GaAs)_m/(AlAs)_n$ superlattices occurs⁴⁰ at a critical value of $10 < (m, n) < 12$. For $m \neq n$ and $(m, n) < 15$, on the other hand, the average *Al* mole fraction of the superlattice serves as a rough guideline for determining the type I or type II behaviour, similar to the ternary $Al_xGa_{1-x}As$ alloy. If the average *Al* mole fraction is smaller than $x = 0.4$, the superlattice exhibits type I behaviour, and in all other cases it behaves as a type II (indirect-gap) material³⁷. Therefore, the $(GaAs)_2/(AlAs)_1$ and $(GaAs)_3/(AlAs)_1$ UTLS are of type I, while the $(GaAs)_2/(AlAs)_2$, $(GaAs)_2/(AlAs)_3$ and $(GaAs)_1/(AlAs)_2$ UTLS are of type II behaviour⁴¹.

The assignment of either type I or type II behaviour to the respective superlattice configuration can be made by careful evaluation of the low-temperature photoluminescence (PL) and photoluminescence excitation (PLE) spectra⁴¹. Figure 9 shows the representative PL and PLE spectra from both types of $(GaAs)_m/(AlAs)_n$ SPS and UTLS. In the type I $(GaAs)_{15}/(AlAs)_{15}$ SPS, the lowest confined *GaAs* Γ -conduction band

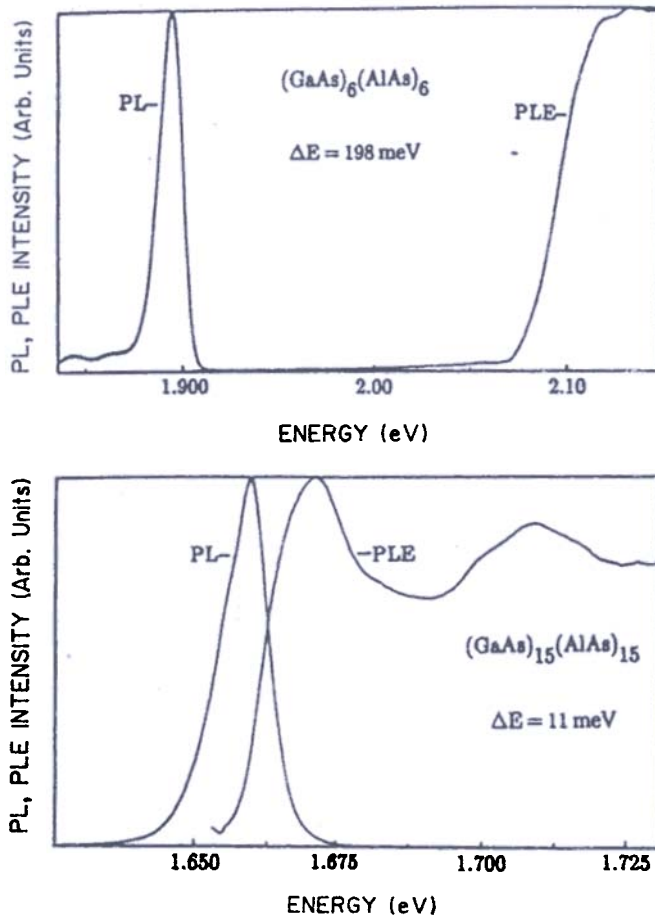


Figure 9. Low-temperature PL and PLE spectra of $(\text{GaAs})_m/(\text{AlAs})_n$ superlattices of type I (bottom) and type II (top) behavior⁴².

state is lower in energy than the lowest confined conduction band states which originate from the X -conduction band minima of the AlAs barriers. The PLE spectrum of Fig. 9(a) exhibits a low-energy onset at about 1.66 eV, and we observe the well-known structure corresponding to the heavy- and light-hole exciton. The PL appears at the low-energy tail of the PLE spectrum, and the Stokes shift between the PL and PLE maxima amounts to 11 meV. Time-resolved PL measurements on type I $(\text{GaAs})_m/(\text{AlAs})_n$ SPS and UTLS with different (m, n) values reveal a continuous decrease of the luminescence decay time with decreasing (m, n) down to values of a few hundred picoseconds for the $(\text{GaAs})_3/(\text{AlAs})_1$ UTLS. This phenomenon is caused by the increase of the radiative (and nonradiative) recombination rates due to localisation in agreement with previous measurements on $\text{GaAs}/\text{Al}_x\text{Ga}_{1-x}\text{As}$ multi-quantum wells.

As an example of the characteristic type II behaviour, the PL and PLE spectra⁴¹ of a $(\text{GaAs})_6/(\text{AlAs})_6$ UTLS is shown in Fig. 9(b). The main PL peak is located at about 1.9 eV, and weaker bands arising from phonon-assisted transitions (phonon replica) appear at lower energy. The PL is attributed to recombination of excitons formed from electrons at X , in the AlAs barriers and holes at Γ in the GaAs wells (Fig. 8). The PLE spectrum shows a steep increase at about 2.08 eV which is attributed to the onset of direct absorption involving electron and hole states both at Γ in the GaAs well (Fig. 8). In the range between 1.9 and 2.08 eV the PLE signal is weak, reflecting the weak strength of the 'spatially' indirect transitions of electrons from a valence band state at Γ in the GaAs into a conduction band state in the AlAs which originates from the X conduction band minima. The features related to light and heavy hole excitons of the direct Γ - Γ transitions (around

2.1 eV in Fig. 9(b)) are always strongly damped in type II superlattices due to the short lifetime of these excitons. The PL decay in type II superlattices is slower by orders of magnitude. In addition, we observe very fast high-energy luminescence transitions in the type II structures due to the recombination of nonthermalised electrons in the *GaAs* layers. However, this PL feature rapidly disappears and thus indicates an extremely fast scattering of electrons from *P*-like conduction band states in the *GaAs* into *X*-like states in the *AlAs* with characteristic time constants considerably smaller than 20 ps. It is finally important to note that the type II (*GaAs*)₂/*(AlAs)*₂ UTLS, although of average composition *Al*_{0.5}*Ga*_{0.5}*As*, exhibits electronic properties totally different from the random ternary alloy.

In the (*GaAs*)_{*m*}/*(AlAs)*_{*n*} SPS and UTLS the minority carrier lifetimes can be tailored within the range of several hundred ps to several μs or even ms simply by selecting the appropriate superlattice configuration during MBE growth. This unique feature opens up a new field of application of these artificially-layered semiconductor structures in nonlinear photonic and optoelectronic devices⁴¹.

4. DELTA-DOPING IN *GaAs* AND *Al_xGa_{1-x}As*

The method of delta-doping also called monolayer atomic plane or sheet doping, is used to obtain doping profiles with atomic layer precision during MBE growth of *GaAs* and *Al_xGa_{1-x}As* layers⁴². The basic concept of delta-doping is illustrated in Fig. 10. Here the dopant atoms of silicon are confined to one atomic plane. The ionised impurity donor

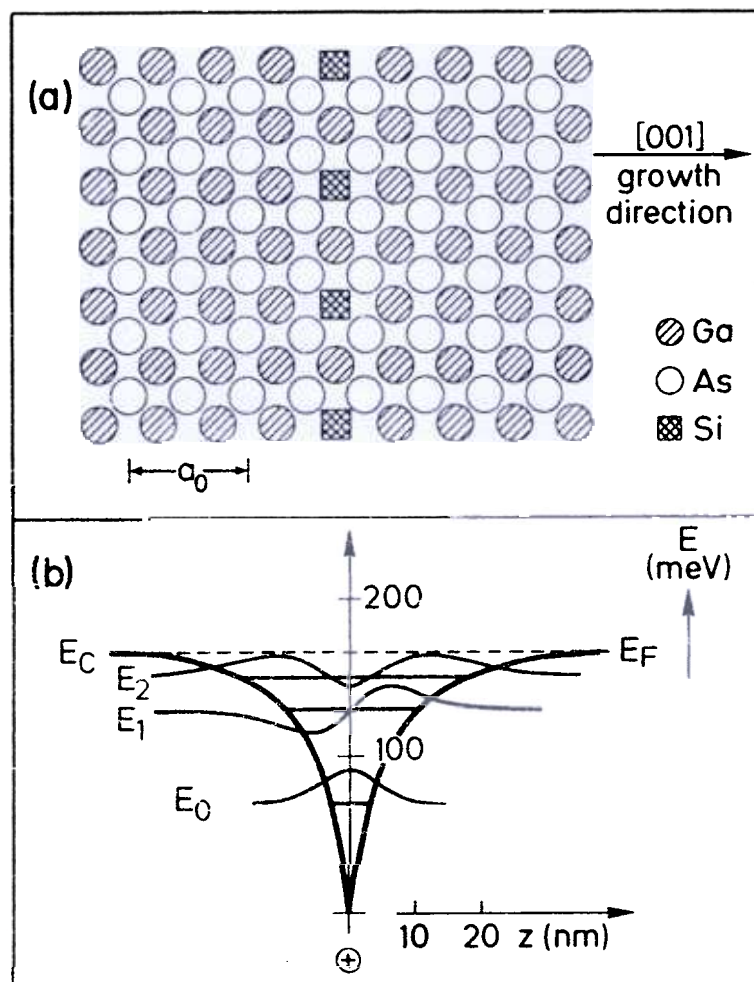


Figure 10. (a) Schematic illustration of *Si* delta-doping in *GaAs* with the dopant atoms confined to a (001) atomic plane, and (b) sub-band energies and wavefunctions in the *V*-shaped potential well.

density generates a V -shaped potential well. The electrons remain close to the parent ionised atoms in the V -shaped potential well and form a quasi-2-DEG. In the potential well their motion is restricted to the direction perpendicular to the wells and hence their energies are quantised into 2-D sub-bands.

The delta-doping profiles of Si and Be are obtained through the interruption of growth of the $GaAs$ or $Al_xGa_{1-x}As$ host crystal by closing the Ga (and Al) shutter and leaving the As shutter open. The ' As -stabilised' reconstruction is thus maintained while the shutter of the respective dopant effusion cell is opened for a certain time interval. In this dopant growth mode the host crystal does not grow. To continue the growth of $GaAs$ or $Al_xGa_{1-x}As$, the dopant shutter is closed and the Ga (and Al) shutter is opened again. The concept of delta-doping can be utilised to fabricate a variety of new device structures and to improve the properties of existing device structures.

As the level of integration proceeds towards ultra large scale integration (ULSI), the gate length of the metal semiconductor field-effect transistor (MESFET) would continue to reduce. For an optimised performance of a MESFET, it is necessary that it has a high sheet carrier density, a high low field mobility and a high saturation velocity⁴³. According to the well-known model⁴³ for the MESFET, as the gate length $L_g \rightarrow 0$, $g_m = \epsilon v_s w_g / d$, where g_m is the intrinsic transconductance, ϵ is the permittivity, v_s is the saturated velocity, w_g is the gate width and d is the distance of the Schottky gate from the position of the sheet carrier concentration. It is clear from this equation that in order to obtain high values of transconductance g_m , it is necessary to have as low a value of d as possible. In a HEMT structure the distance d is about⁴⁴ 60 nm. On the other hand, in principle the delta-doped layer can be placed at any distance below the Schottky gate. But taking into account the surface Fermi level pinning effects, there is a practical limit to the distance at which the delta-doped layer can be placed below the surface. Isibashi *et al.*⁴⁵ have shown that using a double delta-doped structure, the ultrathin channeled MESFET with intrinsic transconductance of 400 ms/mm can be fabricated. Figure 11 shows a

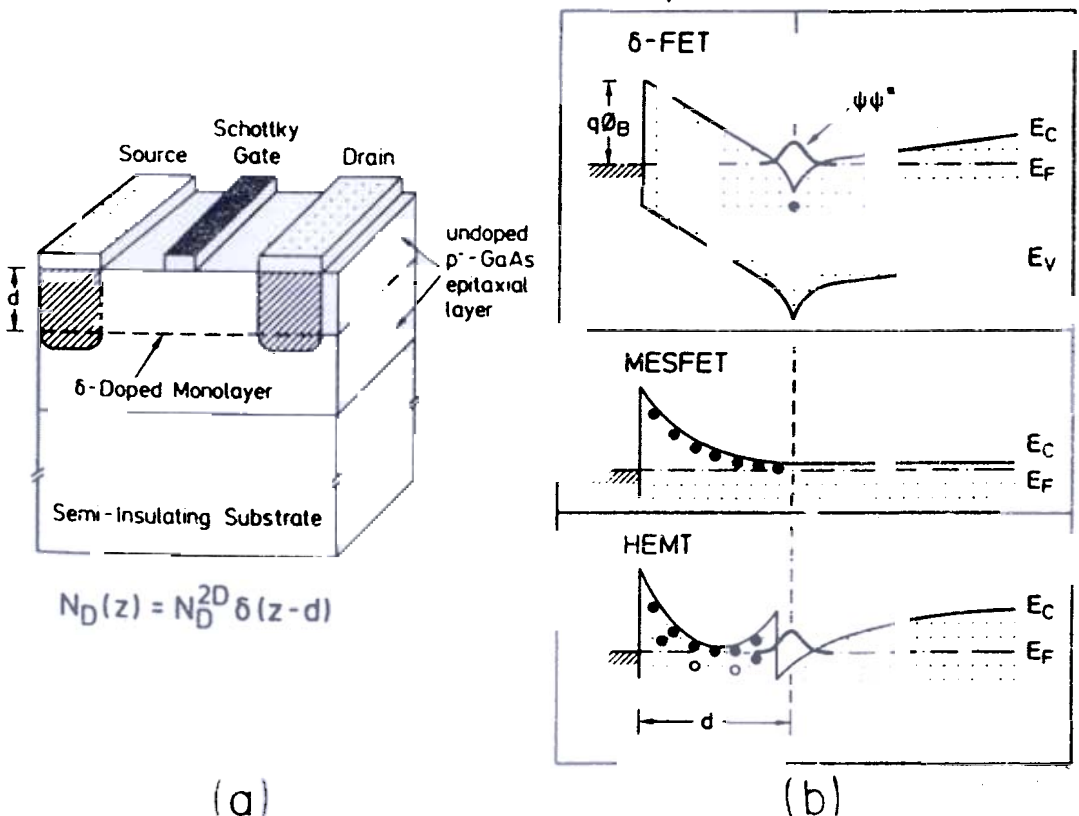


Figure 11. Schematic of the Si delta-doped $GaAs$ MESFET structure (left) and conduction band edge diagram for different types of FETs (right).

schematic of the MESFET structure and the band diagrams for different types of doped layers in FETs.

Now we consider the structures in which high carrier mobilities can be obtained utilising delta-doping. Due to the close proximity of the ionised impurity and the carriers, the Hall mobility of the 2-DEG in the delta-doped layer is comparable to the homogeneously doped material of equivalent doping concentration. Therefore, the delta-doping has to be combined with that of selectively-doped heterostructures for an effective spatial separation of the 2-DEG from the atomic plane of the ionised impurities in order to achieve the high carrier mobilities. It is well-known that in the selectively-doped structure of $GaAs/Ga_xAl_{1-x}As$ very high mobilities can be obtained⁴⁶. It has become possible recently⁴² to combine the concept of delta-doping and modulation-doping to achieve higher values of mobilities and sheet carrier concentration. The band diagram for the conventional modulation-doped structure is shown in Fig. 12(a). The $Al_xGa_{1-x}As$ layer is doped homogeneously with Si and the $GaAs$ is separated from the doped $Al_xGa_{1-x}As$

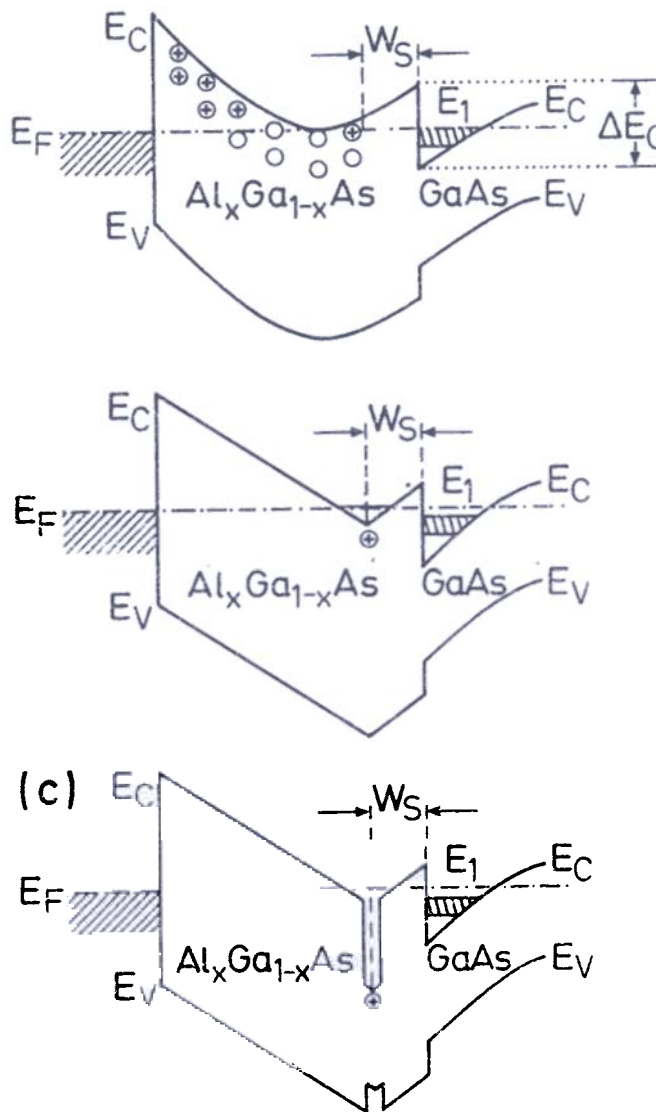


Figure 12. Schematic real-space energy band diagrams of (a) conventional selectively-doped $GaAs/Al_xGa_{1-x}As$ heterostructure (W_S is the spacer thickness, E_C and E_V are the conduction and valence band edges, respectively, E_C is the conduction band discontinuity at the $GaAs/Al_xGa_{1-x}As$ interface, E_F is the Fermi level, E_1 is the first sub-band in the triangular potential well at the interface), (b) the selectively-doped structure in which the $Al_xGa_{1-x}As$ is delta-doped at a distance W_S from the interface, and (c) a structure as in (b) where the delta-doped layer in the $Al_xGa_{1-x}As$ is embedded in the centre of a 2 nm $GaAs$ quantum well.

layer by a spacer layer of thickness W_s . The electrons are separated from the ionised impurities and are located in the sub-bands at the hetero-interface. The next obvious step is to introduce the delta-doping in the $Al_xGa_{1-x}As$ layer. The band diagram of such a structure is shown in Fig. 12(b). The delta-doping in $Al_xGa_{1-x}As$ is separated from the hetero-interface by W_s . This separation produces a strong mobility enhancement. In this structure, it is easy to obtain high charge carrier densities combined with a strongly enhanced mobility even at room temperature. Such structures are extremely useful for the fabrication of HEMTs. A still further improvement is obtained if the atomic plane of doping in $Al_xGa_{1-x}As$ is surrounded on each side by 1 nm GaAs so that it is actually embedded in a 2 nm wide GaAs quantum well. The band diagram of such a structure is shown in Fig. 12(c). Using this modified structure mobilities of $1 \times 10^6 \text{ cm}^2 \text{ V}^{-1} \text{ s}^{-1}$ have been obtained⁴². This increase in carrier mobility is due to the different nature of screening of impurities. In addition, the undesired effect of persistent photoconductivity due to deep donors in $Al_xGa_{1-x}As$ is also significantly reduced in this structure because the $Al_xGa_{1-x}As$ barrier in this is essentially undoped.

In order to achieve high mobilities in the simple delta-doped structure shown in Fig. 13(a), the doping in the delta layer is required to be high in order that there are enough carriers remaining after being taken away by the surface states which pin the Fermi level at the surface. As the delta-doping density is increased, the impurity scattering also increases and the values of mobility obtained are not very high. An improvement over this structure

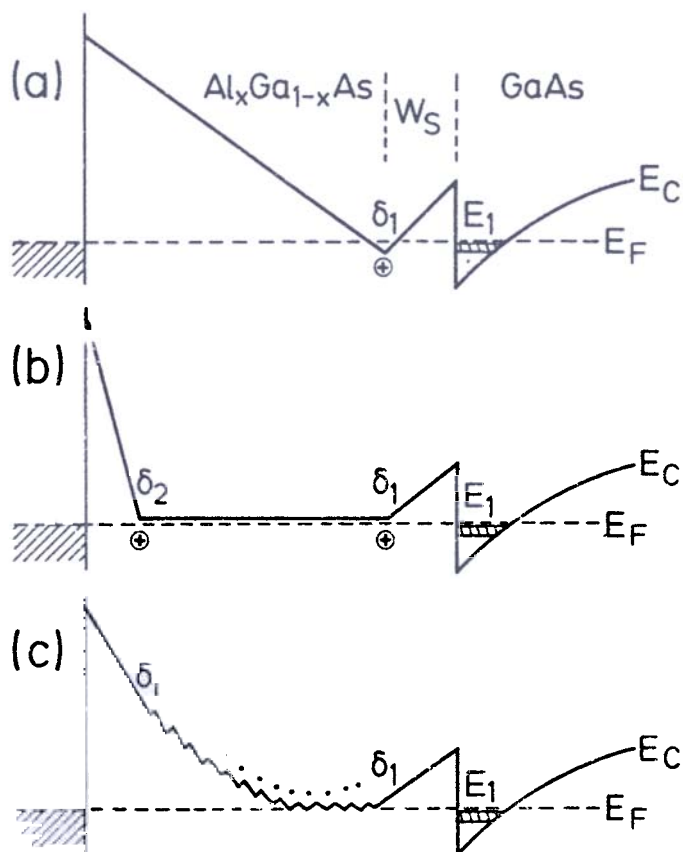


Figure 13. Energy band diagram of a selectively-doped (a) heterostructure in which the $Al_xGa_{1-x}As$ is delta-doped (marked δ_1) at a distance W_s from the interface, (b) structure in which the $Al_xGa_{1-x}As$ contains two delta-doped layers (the delta-doped layer marked δ_1 is at a distance W_s from the hetero-interface and provides the carriers to the 2-DEG and the delta-doped layer marked δ_2 near the surface is to provide electrons to the surface states which pin the Fermi level at the surface), and (c) structure in which the $Al_xGa_{1-x}As$ contains several delta-doped layers. This structure gives the highest mobility values reported so far.

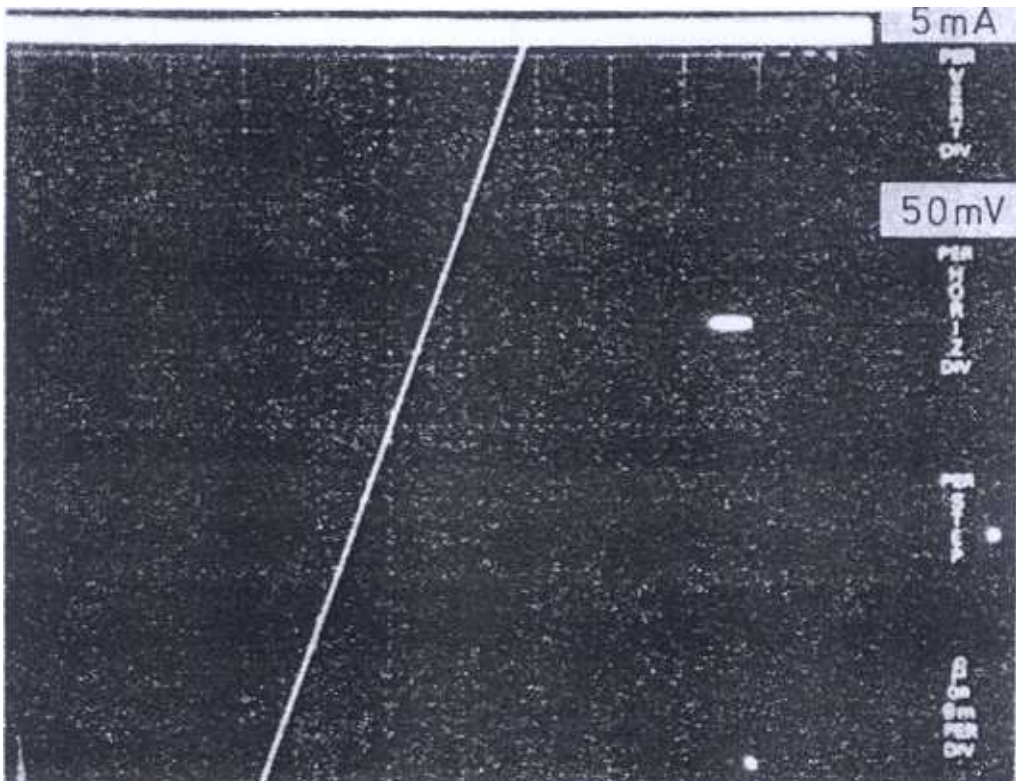
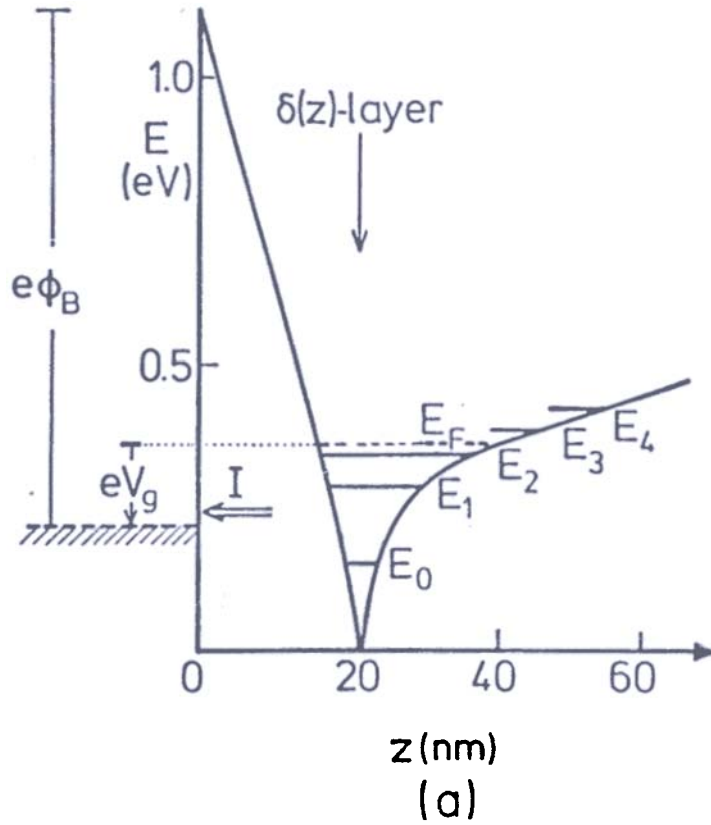


Figure 14. (a) Schematic conduction band diagram of a metal-*n-GaAs* (delta-doped) structure in which the delta-doped layer is 20 nm below the metal-semiconductor interface. ϕ_B is the barrier height, V_g is the applied voltage, and I is the current. E_1, E_2, \dots , are the sub-band energies. (b) Current-voltage characteristics of a non-alloyed ohmic contact to delta-doped *n-GaAs* with the Si-delta-doping layer 2.5 nm below the metal gate.

is to place an additional delta-doped layer near the surface (marked δ_2 in Fig. 13(b)) to provide for electrons to the surface states. The delta-doped layer (marked δ_1) which contributes to the 2-DEG can be lightly doped and hence very high carrier mobilities can be obtained. Further improvements can be made by placing several delta-doped layers in $Al_xGa_{1-x}As$ as shown in Fig. 13(c). Using this structure English *et al.*⁴⁷ have obtained mobility value of $5 \times 10^6 \text{ cm}^2 \text{ V}^{-1} \text{ s}^{-1}$ and recently Bell Labs⁴⁸ has reported values of mobility as high as $1 \times 10^7 \text{ cm}^2 \text{ V}^{-1} \text{ s}^{-1}$. So far we have discussed the possibility of engineering the bulk properties of $GaAs$ and $Al_xGa_{1-x}As$ heterostructures by delta-doping.

Now we proceed to show as to how delta-doping can be utilised to alter the surface properties of $GaAs$. Firstly we discuss the formation of non-alloyed ohmic contacts to $GaAs$. The formation of low resistance ohmic contacts is an important step in the fabrication of discrete devices and VLSI. The band diagram of an n -type $GaAs$ with a delta-doped layer at 20 nm from the surface and with a metal layer on top is shown in Fig. 14(a). In order that this contact becomes ohmic it is essential that the height of the tunneling barrier and its width be reduced. This can be achieved by placing several delta-doped layers beneath the surface. Indeed this has been demonstrated by Ploog *et al.*⁴². In the epitaxial

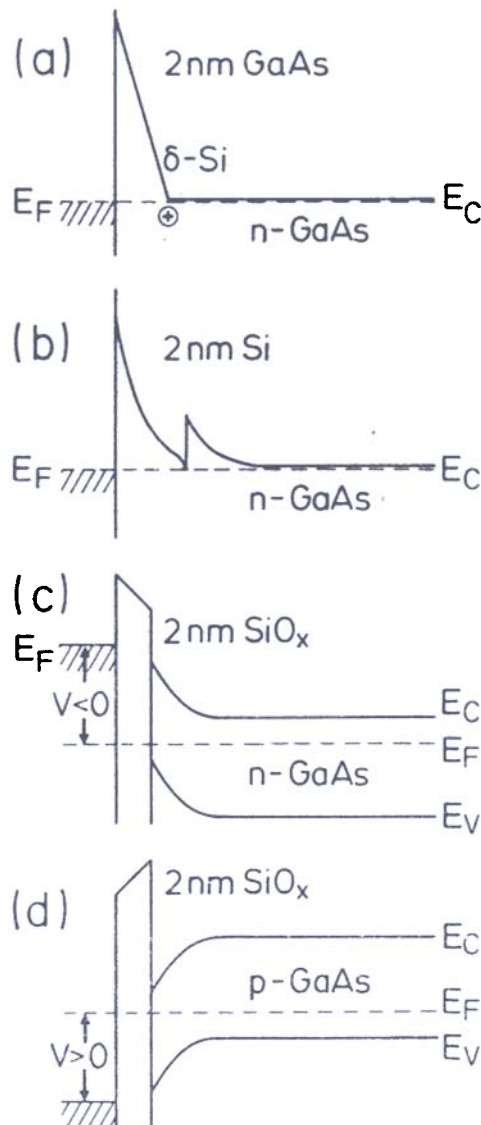


Figure 15. Schematic conduction band diagrams of different configurations of Si -monolayer incorporation into $GaAs$: (a) for nonalloyed ohmic contact, (b) for metal-semiconductor structures with adjustable barrier height, (c) and (d) for metal-insulator-semiconductor structures with a low density of states at the insulator-semiconductor interface.

layer on the substrate a delta-doped layer of $n_s = 1.2 \times 10^{13} \text{ cm}^{-2}$ was grown 2.5 nm below the surface. In order to obtain ohmic contact to the epitaxial layer five additional delta-doped layers separated by 2.5 nm each were grown below the surface. It was found that the evaporation of *Cr/Au* dots on such a structure resulted in non-alloyed ohmic contacts as expected. The current-voltage characteristics of such a structure are shown in Fig. 14(b).

Fabricating an IGFET on *GaAs* has been a long standing problem for the technologists⁴⁹. This has been a difficult problem due to the presence of high density of surface states or interface states between the insulator and *GaAs*. Hence the thermal and anodic oxides of *GaAs* are not highly resistive. Further such oxides are mechanically weak and the Fermi level is pinned near the mid gap. In order to overcome these problems other insulators like *SiO₂* and *Si₃N₄* have been deposited on *GaAs*. However, the attempts until recently have not been very successful in obtaining very good layers of such dielectrics for use in the fabrication MOS devices. Now we discuss the possibility of obtaining a good insulator on *GaAs*. This is done by terminating the growth of *GaAs* by closing the *Ga* shutter and opening the *Si* shutter. The *Si* effusion cell is kept at a very high temperature in order to obtain a high flux of *Si* atoms. The *Si* effusion cell is specially designed⁵⁰ in order to obtain very high temperatures, i.e., as high as 1400°C. The cell uses an elemental pure silicon rod as filament. By passing a high current through this filament very high temperatures of silicon can be obtained which result in a high flux of silicon atoms. The silicon atoms thus deposited on *GaAs* form an epitaxial film of *Si*. When this film is brought in contact with the atmosphere, its surface gets oxidised. A further deposition of *SiO₂* by the conventional means results in an excellent layer of *SiO₂*. The band diagram of *n*-type and *p*-type *GaAs* with an *SiO₂* layer is shown in Fig. 15. Tiwari *et al.*⁵¹ have shown that MOSFETs fabricated with such oxides on *GaAs* show excellent characteristics.

5. CONCLUSION

After a brief discussion of the fundamental aspects of MBE to fabricate custom-designed microstructures, we have described two prototype artificially-layered III-V semiconductors in which the concept of microscopical structuring of solids is scaled to its ultimate physical limit normal to the crystal surface, i.e., *GaAs/AlAs* ultrathin-layer superlattices and delta- (or monolayer) doping in *GaAs* and *GaAs/Al_xGa_{1-x}As* structures. In both the (*GaAs*)₁/*(AlAs)*₁ monolayer superlattice and in the delta-doped *GaAs/Al_xGa_{1-x}As* the characteristic material length normal to the surface has reached a spatial extent of less than the lattice constant. Due to the indirect-gap nature of the constituent *AlAs* layers, the (*GaAs*)_{*m*}/*(AlAs)*_{*n*} UTLS exhibit novel optical properties. The minority-carrier lifetimes can be tailored within the range of several hundred picoseconds to several microseconds simply by the appropriate design of the superlattice configuration during MBE growth. This unique feature opens up a new field for application of these structures in lasers and in nonlinear photonic and optoelectronic devices.

The incorporation of a narrow buried doping channel in delta-doped *GaAs* layers and in *GaAs/Al_xGa_{1-x}As* structures leads to a major improvement of the electrical properties. Based on this concept, nonalloyed ohmic contacts to *GaAs*, FETs with very high transconductance and excellent current driving capabilities, and unpinned *GaAs* surfaces for MOS devices have been fabricated. Finally, the record electron mobility in selectively-doped *GaAs/Al_xGa_{1-x}As* heterostructures as high as $10^7 \text{ cm}^2 \text{V}^{-1} \text{ s}^{-1}$ has also been achieved with the concept of *Si* delta-doping.

ACKNOWLEDGEMENTS

Part of this work was sponsored by the Bundesministerium für Forschung und Technologie of the Federal Republic of Germany.

REFERENCES

1. Cho, A.Y. & Arthur, J.R., *Progr. Solid State Chem.*, **10** (1975), 157.
2. Ploog, K., *Angew. Chem. Int. Ed. Engl.*, **27** (1988), 593.
3. Sakaki, H., *In Proc. Int. Symp. on Foundations of Quantum Mechanics*, Tokyo, 1983, p. 94.
4. Capasso, F., *Science*, **235** (1987), 172.
5. Gossard, A.C., *Treat. Mater. Sci. Technol.*, **24** (1981), 13.
6. Joyce, B.A., *Rep. Progr. Phys.*, **48** (1985), 1637.
7. Chang, L.L. & Ploog, K., (Eds.), *Molecular Beam Epitaxy and Heterostructures*, (Martinus Nijhoff, Dordrecht), 1985, NATO Advance Science Institute Series E 87.
8. Parker, E.H.C., (Ed.), *The Technology and Physics of Molecular Beam Epitaxy*, (Plenum Press, New York), 1985.
9. Sakamoto, T., Funabashi, H., Ohta, K., Nakagawa, T., Kawai, N.J., Kojima, T. & Bando, K., *Superlatt. Microstruct.*, **1** (1985), 347.
10. Joyce, B.A., Dobson, P.J., Neave, J.H., Woodbridge, K., Zhang, J., Larsen, P.K. & Bölger, B., *Surf. Sci.*, **168** (1986), 423.
11. Suzuki, Y. & Okamoto, H., *J. Appl. Phys.*, **58** (1985), 3456.
12. Tanaka, M., Sakaki, H. & Yoshino, J., *Jpn. J. Appl. Phys.*, **25** (1986), L155.
13. Voillot, F., Madhukar, A., Kim, J.Y., Chen, P., Cho, N.M., Tang, W.C. & Newman, P.G., *Appl. Phys. Lett.*, **48** (1986), 1009.
14. Tapfer, L. & Ploog, K., *Phys. Rev.*, **B 33** (1986), 5565.
15. Meirav, U., Heiblum, M. & Stern, F., *Appl. Phys. Lett.*, **52** (1988), 1268.
16. Lang, D.V., Logan, R.A. & Jaros, M., *Phys. Rev.*, **B 19** (1979), 1015.
17. Schubert, E.F. & Ploog, K., *Phys. Rev.*, **B 30** (1984), 7021.
18. Morgan, T.N., *Phys. Rev.*, **B 34** (1986), 2664.
19. Dingle, R., Logan, R.A. & Arthur, J.R., *Inst. Phys. Conf. Ser.*, **33a** (1977), 210.
20. Camras, M.D., Holonyak, N., Hess, K., Coleman, J.J., Burnham, R.D. & Scifres, D.R., *Appl. Phys. Lett.*, **41** (1982), 317.
21. Fujiwara, K., Oppolzer, H. & Ploog, K., *Inst. Phys. Conf. Ser.*, **74** (1985), 351.
22. Ploog, K., Ohmori, Y., Okamoto, H., Stolz, W. & Wagner, J., *Appl. Phys. Lett.*, **47** (1985), 384.
23. Wagner, J., Stolz, W., Knecht, J. & Ploog, K., *Solid State Commun.*, **57** (1986), 781.
24. Fujiwara, K., De Miguel, J.L. & Ploog, K., *Jpn. J. Appl. Phys.*, **24** (1985), L405.
25. Deveaud, B., Chomette, A., Lambert, B., Regreny, A., Romestain, R. & Edel, P., *Solid State Commun.*, **57** (1986), 885.

26. Nakamura, A., Fujiwara, K., Tokuda, Y., Nakayama, T. & Hirai, M., *Phys. Rev.*, **B 34** (1986), 9019.
27. Fujiwara, K., Nakamura, A., Tokuda, Y., Nakayama, T. & Hirai, M., *Appl. Phys. Lett.*, **49** (1986), 1193.
28. Fujii, T., Hiyamizu, S., Yamakoshi, S. & Ishikawa, T., *J. Vac. Sci. Technol.*, **B 3** (1985), 776.
29. Ploog, K. & Fischer, A., *Appl. Phys. Lett.*, **48** (1986), 1392.
30. Coleman, J.J., Dapkus, P.D., Laidig, W.D., Vojak, B.A. & Holonyak, N., *Appl. Phys. Lett.*, **38** (1981), 63.
31. Tokuda, Y., Ohta, Y.N., Fujiwara, K. & Nakayama, T., *J. Appl. Phys.*, **60** (1986), 2729.
32. Baba, T., Mizutani, T. & Ogawa, M., *Jpn. J. Appl. Phys.*, **22** (1983), L627.
33. Blood, P., Fletcher, E.D. & Foxon, C.T., *In Proceedings of the SPIE—International Society for Optical Engineering*, Vol. 861 (SPIE, Bellingham), 1987, p. 61.
34. Hayakawa, T., Suyama, T., Takahashi, K., Kondo, M., Yamamoto, S. & Hijikata, T., *Appl. Phys. Lett.*, **49** (1986), 636.
35. Nakayama, M., Kubota, K., Kato, H., Chika, S. & Sano, N., *Solid State Commun.*, **53** (1985), 493.
36. Isu, T., Jiang, D.S. & Ploog, K., *Appl. Phys.*, **A 43** (1987), 75.
37. Nagle, J., Garriga, M., Stolz, W., Isu, T. & Ploog, K., *J. Physique*, **48** (1987), Colloque C5-495.